Statistics of the Intense Current Structure in the Dayside Magnetopause Boundary Layer

Hengyan Man[1,2], Meng Zhou[2,3*], Zhihong Zhong[2,4], Xiaohua Deng[2], Haimeng Li[2]

[1]School of Resources Environmental and Chemical Engineering, Nanchang University, Nanchang, China

[2]Institute of Space Science and Technology, Nanchang University, Nanchang, China

[3]Department of Physics, School of Science, Nanchang University, Nanchang, China

[4]School of Materials Science and Engineering, Nanchang University, Nanchang, China

Key points:

1. Most ICS at the magnetopause boundary layer have a temporal duration of less than 1 s and thickness of less than 1 di.
2. The ICS has a higher occurrence rate close to Earth and in the dusk sector near the meridian.
3. The ICS is important in the non-ideal energy conversion in the magnetopause boundary layer.

Abstract

This paper presents a comprehensive study of the intense current structure (ICS) at the dayside magnetopause, by using the high-resolution data from the Magnetospheric Multiscale (MMS) mission. About 3,600 ICSs with current density exceeding 1.2 $\mu A/m^2$ have been detected during phase 1a and 1b within the magnetopause boundary layer (MBL). We find that most ICSs have a temporal duration of less than 1 second and thickness of less than one ion inertial length. The number of ICSs decreases with the thickness increasing from the electron-scale to the ion-scale. The occurrence rate of the ICS is relatively higher close to Earth and in the dusk sector near the meridian, probably caused by the large solar wind dynamic pressure. In a local boundary normal coordinate system, the occurrence rate is higher on the magnetosheath side. For most ICSs, the current is carried by electrons. The perpendicular current is larger than the parallel current for more ICSs. The energy conversion $J \cdot E$ is primarily through the perpendicular current and electric field, while the non-ideal energy conversion $J \cdot E'$ is mainly dominated by the parallel component. ICSs provide much stronger energy conversion and dissipation compared to the ambient plasma in the MBL. This study improves our understanding of the characteristics of the ICS and its role in solar wind-magnetosphere coupling.

Plain Language Summary

Current sheet is the hotbed for various instabilities and an important site for energy exchange between electromagnetic fields and plasmas. Current structures with electric current density exceeding 1 μA/m2 have frequently observed by the Magnetospheric Multiscale mission at the dayside magnetopause boundary layer. Important features of these intense current structures, such as the occurrence rate, current carrier, contribution to energy conversion, are not clear. This paper presents a comprehensive analysis of more than three thousand intense current structures at the magnetopause. We show that most of these current structures are extremely short in time domain and have thicknesses less than the ion inertial length. Moreover, they play important roles in energy dissipation within the boundary layer. These results are of great help in understanding the characteristics of the intense current structures and their role in the solar wind-magnetosphere coupling.

1. Introduction

Current sheet is ubiquitous in plasmas and is important for energy conversion between electromagnetic fields and plasma. Macroscopic energy release and transport in the magnetosphere are essentially regulated by two large-scale current sheets: the magnetopause current sheet and the magnetotail neutral sheet. In turbulent plasma, such as

magnetosheath and transition region of the bow shock, small-scale current sheets are suggested to be important for dissipating energy stored in the turbulent electromagnetic fields (Retinò et al., 2007; Phan et al., 2018; Wang et al., 2019).

Various instabilities are born in current sheet. One typical example is the tearing instability, which is responsible for triggering magnetic reconnection. Lower hybrid drift instability (LHDI) is also a ubiquitous instability in current sheet, where the diamagnetic drift usually exists to provide the free energy for the LHDI. The fastest growing electrostatic LHDI is confined at the boundary and electromagnetic mode can penetrate into the central current sheet (Daughton, 2003; Zhou et al., 2009; 2014). Fluid-type instabilities which are probably induced by LHDI, such as the drift-kink instability, could disrupt the current sheet significantly along the current direction (Daughton, 1999; Lapenta et al., 2003; Moser and Bellan., 2012).

The neutral sheet is formed between the stretched anti-parallel magnetic fields in the magnetotail (Erickson and Wolf, 1980; Schindler and Birn, 1982). Magnetic reconnection occurs in the neutral sheet when its thickness goes down to the ion or electron inertial length (Pulkkinen et al., 1999; Pulkkinen and Wiltberger, 2000; Lu et al., 2020). In situ observations have identified well-structured Hall electromagnetic fields consistent with fast reconnection theory in the magnetotail (Borg et al.,

2005; Eastwood et al., 2007). Usually, the neutral sheet is not a plane but deforms substantially with its normal deviates from Z direction in the Geocentric Solar Magnetospheric (GSM) coordinates toward the dawn-dusk direction (Sergeev et al., 2003). Moreover, it occasionally exhibits a bifurcated structure, that is, the current density peaks off-center (e.g., Runov et al., 2003).

Another important current sheet in the magnetotail is the dipolarization front, which is a vertical current sheet with its normal mainly in the X-Y plane. Dipolarization front is an important boundary layer separating the heated plasma from magnetic reconnection and the ambient plasma (Nakamura et al., 2002; Runov et al., 2009; Zhou et al., 2009). It is generally an ion-scale structure, often involving electron-scale sub-structures (Fu et al., 2012; Liu et al., 2018; Pan et al., 2018; Zhou et al., 2019a). Other electron-scale vertical current sheets have also been detected within the turbulent plasma flows driven by magnetic reconnection (Zhou et al., 2019a; 2021), and between the earthward propagating flux rope and geomagnetic field (Man et al., 2018). It is suggested that these vertical current sheets play essential roles in energy conversion during the disturbed magnetotail, such as magnetospheric substorms (Sergeev et al., 2009; Huang et al., 2012; 2015; Vogiatzis et al., 2015; Man et al., 2018).

The magnetopause current sheet is the outer boundary of the

111 magnetosphere, resulting from the interaction between the solar wind
112 plasma and geomagnetic field. It is composed of a diamagnetic current
113 that is perpendicular to the magnetic field, namely the Chapman-Ferraro
114 current (Chapman and Ferraro, 1931), and field-aligned currents, which
115 are important for magnetosphere-ionosphere coupling. As a transition
116 region between the hot-tenuous plasma in the magnetosphere and the
117 cold-dense plasma in the magnetosheath, magnetopause plays a
118 fundamental role in the transport of solar wind plasma into the
119 magnetosphere (Hasegawa, 2012). Pioneer studies using ISEE and
120 AMPTE observations found that the thickness of the magnetopause
121 current sheet is several proton gyro-radii and it is a constantly moving
122 structure with changing velocity (Elphic and Russell, 1979; Berchem and
123 Russell, 1982; Le and Russell, 1994). Ion-scale current sheet is an ideal
124 place for reconnection at magnetopause (Bale et al., 2002; Mozer et al.,
125 2002; Vaivads et al., 2004). However, due to the asymmetric magnetic
126 field and plasma condition across the magnetopause current sheet, the
127 structure of the reconnection layer at magnetopause is distinct from that
128 in the magnetotail (Mozer and Pritchett, 2009). Electron-scale current
129 sheet at the magnetospheric separatrix was also reported (André et al.,
130 2004).

131 Before the MMS era, current density was usually estimated by
132 curlometer technique using simultaneous magnetic field and position

133 measurements from four spacecraft (Dunlop et al., 2002). However, the
134 inter-distance of four Cluster spacecraft is generally larger than the ion
135 inertial length (~ 100 km) at the magnetopause, thus it can resolve only
136 the current structure on the ion-scale. The current density calculated by
137 curlometer technique from Cluster mission is generally less than 1 $\mu A/m^2$,
138 given that a magnetic field change of ~ 30 nT over a typical spacing of
139 Cluster ~ 100 km at the magnetopause.

140 These limitations were overcome by MMS, which is designed to
141 resolve electron-scale physics associated with reconnection (Burch et al.,
142 2016). One powerful ability of MMS is that it can reliably calculate the
143 current density directly from the plasma density and bulk velocity, i.e.,
144 $J = n(V_i - V_e)$ (e.g., Phan et al., 2016; Zhou et al., 2016). Plenty of
145 sub-ion scale current sheets with large current density have been observed
146 by MMS in recent years in different regions, such as the electron
147 diffusion region in the magnetopause and magnetotail (Burch et al., 2016;
148 Nakamura et al., 2018, 2019; Torbert et al., 2018; Zhou et al., 2019b;
149 Burkholder et al., 2020), current filaments within the magnetic flux rope
150 (Eastwood et al., 2016; Hwang et al., 2016; Zhao et al., 2016; Zhou et al.,
151 2017; Man et al., 2018, 2020; Wang et al., 2020). These studies point out
152 that sub-ion scale current sheets are significant for energy conversion and
153 particle acceleration.

154 To have a better understanding of the intense current structure (ICS)

155 at the magnetopause, we have performed a statistical analysis on the scale
156 size, spatial distribution, current carrier and energetics of these ICSs in
157 this paper. We have used the data from the following instruments onboard
158 MMS: The Fluxgate Magnetometer (FGM) provides 3-D magnetic field
159 vectors (Russell et al., 2016; Torbert et al., 2016); The Fast Plasma
160 Investigation (FPI) provides the integrated electron moments with a
161 temporal resolution of 0.03 s and ion moments with a temporal resolution
162 of 0.15 s in burst mode and a temporal resolution of 4.5 s in fast mode
163 (Pollock et al., 2016); The 3-D electric field vectors are provided by the
164 Electric Field Double Probe (EDP) (Ergun et al., 2016; Lindqvist et al.,
165 2016; Torbert et al., 2016).
166

167 ## 2. Database

168 Our database includes all the burst mode intervals (more than 9,000,
169 each interval lasts a few minutes) of MMS during phase 1a (1 September
170 2015 to 7 March 2016) and phase 1b (26 September 2016 to 31 January
171 2017). Here we use data from MMS1 only because of the extremely small
172 spacing among the four spacecraft. The following procedure is performed
173 to select the burst mode intervals within which MMS was in the
174 magnetopause boundary layer (MBL). Fast mode data in these burst
175 intervals are used to determining the MBL.
176 (1) The average radial distance between MMS1 and Earth should be less

than 15 Earth radii (R_E).

(2) The boundary layer is the transition region between magnetosphere and magnetosheath, thus we have removed the intervals when MMS was always inside the magnetosphere or magnetosheath proper. Plasma temperature in the magnetosphere and magnetosheath is obviously different. The energy of the dominant electron population in the magnetosphere is larger than 1 keV, while it is less than 1 keV in the magnetosheath (Pu et al., 2013). Accordingly, we use the parameter α, which is defined as the ratio of the integrated differential electron flux in the low energy range (30 eV to 800 eV) and high energy range (1 keV to 25 keV). The lower bound for the low energy range is set as 30 eV to remove possible contamination by photoelectrons below 30 eV. Burst mode intervals containing MBL crossings are picked out by requiring $1<\alpha<170$. This range is chosen by examining hundreds of burst mode intervals by eyes. α is less than 1 when MMS1 is inside the magnetosphere and $\alpha>170$ when MMS is in the magnetosheath proper. However, burst intervals with $\alpha>170$ may record one or more magnetopause crossings. Hence, we retain this burst mode interval if there are more than 3 points (~ 13 s) with $N_e < 2$ cm^{-3} within it, which means that there is at least one magnetopause crossing.

(3) MMS occasionally crossed the bow shock and entered the solar wind, where the criteria listed in procedures (1) and (2) may be satisfied. Hence,

199 we further require that the average ion velocity in the X direction is larger
200 than -200 km/s to remove the intervals in the solar wind. In addition, the
201 burst interval involving bow shock is removed if the number of points
202 with N_e>100 cm^{-3} exceeds 3.

203 In total, we have selected about 5,700 burst mode intervals that
204 contain the MBL following the above procedures. Figure 1A shows one
205 of these qualified burst mode intervals. We see that MMS1 passed
206 through the MBL from the magnetosphere to the magnetosheath from
207 approximately 23:24 UT to 23:27 UT on December 11, 2015. During this
208 interval, MMS was located around (X= 8.5, Y= -4.5, Z= -1.1) R_E. MMS
209 observed a stable magnetic field pointing northward and dawnward
210 (Figure 1a) and tenuous-hot plasma (N< 2cm^{-3}, T_i > 3 keV, T_e > 1 keV) in
211 the magnetosphere (Figure 1c, 1f and 1g). Ions are mostly above 1 keV
212 except for some cold ions observed around 23:25:15 UT (Figure 1h). On
213 the contrary, the magnetic field exhibits stronger fluctuations (Figure 1a)
214 in the magnetosheath proper, where N_e is up to 30 cm^{-3} (Figure 1c), and
215 the ion and electron temperature are much lower than that in the
216 magnetosphere (Figure 1f and 1g). Electrons with energy above 1 keV
217 almost disappear in the magnetosheath (Figure 1i). The region between
218 the two red dashed lines is the MBL, within which N_e rises to about 10
219 cm^{-3} from the magnetosphere. Particles from the magnetosphere and
220 magnetosheath are mixed in the MBL, which is evident in Figure 1i that

low-energy and high-energy electrons coexist in this region.

Figure 2 shows the probability distribution of the total current density ($|Jp| = \sqrt{Jp_x^2 + Jp_y^2 + Jp_z^2}$) in the burst mode intervals we have picked out. Each point is calculated by using the plasma moments at a cadence of 0.03 s and there are about 24 million samples in total. The distribution shows that the number of data points decreases as the current density increases. Here we choose 1.2 μA/m^2 as the threshold for the ICS, i.e., if |Jp| is larger than 1.2 μA/m^2 , then it will be identified as an ICS. 1.2 μA/m^2 is about ten times the standard deviation of the Jp distribution shown in Figure 2. This value is also approximately the lowest value of the top 0.05% current density. The boundary of each ICS is determined by the average value of |Jp| in the corresponding burst mode interval. Furthermore, we have removed the data with large measurement uncertainties by getting rid of the ICSs with an average plasma density of less than 5 cm^{-3} (Webster et al., 2018). Figure 1B illustrates three ICSs found within the black frame in Figure 1A. They are located at the edge of the MBL where the high energy (> 1 keV) electron flux decreases significantly. The upper horizontal line in Figure 1p marks the threshold of 1.2 μA/m^2, and the lower horizontal line represents the average $|J_p|$ (~ 0.16 μA/m^2) within the entire burst mode interval. We see that these ICSs correspond to prominent increases in the electron velocity and fluctuations in the magnetic field. These three ICSs were detected within

243 3 seconds. Overall, we have identified 3,624 ICSs within the MBL. The
244 characteristics of these ICSs from a statistical perspective are illustrated
245 in detail in the following section.
246
247 # 3. Results
248 ## 3.1. Duration and Thickness
249 Figure 3a presents the probability distribution function (PDF) of the
250 temporal duration of these ICSs. The PDF increases from 0.03 s to 0.15 s
251 and then decreases as the increment of the duration. The PDF reaches a
252 peak at the duration of 0.15s. Most ICSs (> 88%) have a duration of less
253 than 2 seconds and the average duration is about 1 second.
254
255 In order to calculate the thickness, we estimate the moving velocity
256 of these structures by the timing analysis (Russell et al., 1983). We chose
257 the magnetic field component which has the maximum variation
258 corresponding to the ICS to do the timing analysis. Considering that the
259 scale of the ICS may be smaller than the spacecraft spacing such that it
260 was not observed by all the four satellites, the thicknesses of some ICSs
261 cannot be estimated. We have also removed the ICSs with the
262 cross-correlation coefficient of the magnetic field among the four
263 spacecraft is less than 0.9. Consequently, there are 2,538 ICSs whose
264 thickness can be reliably estimated from the timing analysis. The PDF of
265 the thickness is shown in Figure 3b. The thickness has been normalized to

the local ion inertial length d_i, which is calculated by using the average plasma density within the ICS. It shows that the thickness of the ICS ranges mainly from tens d_e to near 10 d_i. The PDF almost monotonically decreases from the electron-scale to the ion-scale. We find that most ICSs are below 1 d_i and the average thickness is about 2 d_i.

3.2 Spatial Occurrence Rate

Figure 4 shows the spatial distribution and occurrence rate of the ICSs at the equatorial plane as a function of L and MLT ($L = \sqrt{x^2 + y^2}$, where x, y is the coordinate in GSM coordinates; MLT represents the magnetic local time). L and MLT are calculated by the International Geomagnetic Reference Field (IGRF) and T96 external model (Tsyganenko, 1995). We interpolate the position data into the cadence of the current density, which is 0.03 s. The spatial distribution of the ICSs is demonstrated in Figure 4a. There are nearly 0.12 million samples inside the ICSs. To get the occurrence rate, the spatial distribution of these ICSs is divided by the total samples in the burst mode in the MBL, which has a total of 24 million samples (shown in Figure 4b). It is clear from Figure 4 (b) that the trajectory of MMS covers the entire dayside magnetopause during phase 1, from 5 to 19 in MLT. In order to reduce the uncertainties caused by too few samplings, the bins where the number of samples below 500 are removed. A relatively high occurrence rate occurs around

L = 8-10 and MLT =12-15, which means that the ICSs preferentially occur close to Earth and in the dusk sector, though the dawn-dusk asymmetry is weak.

Besides the spatial distribution in a global fixed coordinate, we are also interested in its spatial distribution in a local coordinate to investigate its connection with magnetic reconnection at the magnetopause. Here we have transformed the vectors into a local boundary normal coordinate (**LMN**) system by using Shue Model (Shue et al.,1997). **N** is normal to the magnetopause, $\mathbf{M}=\mathbf{N}\times\mathbf{Z}_{GSM}$, and $\mathbf{L}=\mathbf{N}\times\mathbf{M}$. The distribution of the ICSs as a function of B_L and V_{iL} is displayed in Figure 5(a). We have also transformed all the data in the selected burst intervals into this local coordinate, the result is shown in Figure 5(b). The distribution of the total sample shown is mostly concentrated near -200 to 150 km/s of V_{iL}, in the range of 0-50 nT of B_L. Figure 5c presents the occurrence rate in this coordinate system. We have deleted the bins in Figure 5c with corresponding samples less than 500 in Figure 5b. We see that the ICSs have a higher occurrence rate on the side with $B_L<0$, i.e., the magnetosheath side with respect to the central current where $B_L=0$, and southward of the X-line where $V_{iL}<0$.

3.3 Current Carrier

To compare the contribution of electron and ion current to the total

current, we project the ion current $Jp_i=n_e*V_i$ and electron current $Jp_e=n_e*V_e$ onto the direction of Jp, namely $Jp_i^{'} = Jp_i(cos\theta), Jp_e^{'} = Jp_e(cos\varphi)$, where θ ($\varphi$) is the angle between Jp_i (Jp_e) and Jp (illustrated on top of Figure 6). We calculate the averaged $Jp_i^{'}$ and $Jp_e^{'}$ for each ICS and consider the following three situations.

Case 1: $Jp_i^{'} < 0\ and\ Jp_e^{'} > 0$, i.e., the direction of Jp_i is opposite to that of Jp, while Jp_e is in the same direction as Jp. Hence, the current is obviously carried by electrons.

Case 2: $Jp_i^{'} > 0\ and\ Jp_e^{'} > 0$. In this case, Jp_i is in the same direction as Jp_e. We calculate the absolute ratio of $Jp_i^{'}$ to $Jp_e^{'}$, i.e., $|Jp_i^{'}|/|Jp_e^{'}|$. If the ratio is greater than 1.5, we classify this ICS as an ion-dominated ICS, that is, the current is mainly carried by ions. If the ratio is less than 0.67, the current is mainly carried by electrons. In other cases, we suggest that ions and electrons contribute equally to the total current.

Case 3: $Jp_i^{'} > 0\ and\ Jp_e^{'} < 0$. Case 3 is opposite to case 1. In this situation, the current is mainly carried by ions.

Figure 6 shows the results according to the above classification. There are about 33%, 55% and 12% ICSs in case 1, case 2 and case 3, respectively. More than half of the ICSs in case 2 has a ratio less than 0.67, i.e., dominated by electron current sheet. Therefore, about 68% of the ICSs are mainly carried by electrons and about 22% of the ICSs are mainly carried by ions. For the rest of the ICS (~ 10%), ion and electron

current contribute nearly equally.

3.4 Current Direction

Figure 7 shows the probability distribution of the ratio of the parallel current ($|Jp_{//}|$) to the perpendicular current ($|Jp_{\perp}|$). $Jp_{//} = J \cdot B/|B|$ refers to the current component along the magnetic field, and $Jp_{\perp}$ is the perpendicular current, which is calculated by $|Jp_{\perp}|=|Jp|-|Jp_{//}|$. Here J and B are the averaged value over each ICS. If the ratio is greater than 1.5, we suggest the current is mainly in the field-aligned direction. If it is less than 0.67, then we suggest it is mainly transverse to the magnetic field. If the ratio is between 0.67 and 1.5, then the two components are comparable to each other. It can be seen from Figure 7 that the for 23% of the ICS, the current is mainly in the field-aligned direction, while the current mainly flows perpendicular to the magnetic field for about 45% of the ICS.

3.5 Energy Conversion and Dissipation

Intense currents are usually associated with strong energy conversion, which can be measured by J·E from the Poynting theorem (Yi et al., 2019). Here we investigate whether the parallel or perpendicular current contributes to the energy conversion. Figure 8a presents the probability distribution of the ratio $|J_{//} \cdot E_{//}|/|J_{\perp} \cdot E_{\perp}|$. As in the aforementioned analysis, these values have been averaged over each ICS.

The ratio is classified into 6 bins. The ratio larger than 1.5 indicates that the energy conversion is mainly through the parallel current and electric field. On the other hand, the energy conversion is mainly through the perpendicular current and electric field if the ratio is less than 0.67. We see that for about 26% of the ICSs, J·E is mainly contributed by $J_{//} \cdot E_{//}$. The perpendicular current and electric field dominate the energy conversion for about 55% of the ICSs, while $|J_{//} \cdot E_{//}|$ and $|J_{\perp} \cdot E_{\perp}|$ is comparable for the rest (~ 19%) of the ICSs.

$J \cdot E^{'} = J \cdot (E + Ve \times B)$ is widely used to quantify the non-ideal energy conversion rate in plasma. It is also suggested as a good parameter to locate the dissipation region in reconnection and turbulence (Zenitani et al., 2011; Burch et al., 2016; Fu et al., 2017; Torbert et al., 2018; Hwang et al., 2019; Zhou et al., 2019b). Similar to the analysis of J·E , we decompose J·E' into the parallel and perpendicular components, $J_{//} \cdot E^{'}_{//}$ and $J_{\perp} \cdot E^{'}_{\perp}$, and calculate their ratio, the probability distribution of which is displayed in Figure 8b. We see that J·E' in more than 52% of the ICSs is provided by the parallel current and parallel electric field, and $J \cdot E^{'}$ in about 29% of the ICSs is dominated by the perpendicular current.

4. Discussion

Figure 9 illustrates that the occurrence rate of ICS is relatively high close to Earth. This high occurrence rate may be caused by the

magnetopause compression owing to the enhanced solar wind dynamic pressure (P_{dyn}). Here we compare the P_{dyn} during the interval when the ICSs were observed, denoted as $P_{dyn,ICS}$, to the other times within the MBL when the ICS was not observed, denoted as $P_{dyn,\ 0}$. The solar wind dynamic pressure is directly from the OMNI data (1-min resolution) provided by NASA's Goddard Space Flight Center (King and Papitashvili, 2005). We have selected the P_{dyn} at the nearest moment before the ICS was detected as the $P_{dyn,ICS}$. By comparing the two PDFs (Figure 9), we find that $P_{dyn,ICS}$ are generally larger than $P_{dyn,0}$. This implies that ICS preferentially occurs during large solar wind dynamic pressure, consistent with the spatial occurrence rate shown in Figure 4c that the occurrence rate of the ICS is higher near Earth because the MBL is pushed inward by large solar wind dynamic pressure.

Figure 8 shows an interesting result that the energy conversion J·E is predominately through the perpendicular current and electric field. This is contrary to the energy dissipation $J\cdot E'$ which is dominated by the parallel current and electric field. We note that the contributions from the parallel current are the same for J·E and $J\cdot E'$ since $J\cdot E = J_{//}E_{//} + J_{\perp}E_{\perp}$ and $J\cdot E' = J_{//}E_{//} + J_{\perp}(E_{\perp} + (V * B)_{\perp}$. Therefore, the difference arises from the non-ideal electric field in the perpendicular direction. To reduce $J_{\perp}(E_{\perp} + (V * B)_{\perp}$ in $J\cdot E'$, the convective electric field $E_c = -V_e * B$ must partially cancel the perpendicular electric field $E_{\perp}$, or say, the

perpendicular electric field is primarily the convective electric field. Note that parallel electric field is significant in about one-quarter of ICSs with J·E dominated by $J_{//}E_{//}$.

We further explore the role of the ICSs in energy conversion within the MBL. Figure 10a presents the PDF of J·E in the ICSs (blue curve) and in the ambient plasma excluding the ICSs (black curve). Since the total number of samples for the two curves is different, the two PDFs have been rescaled to match the two peak values. It is shown that the distribution is almost symmetric with respect to J·E=0 by comparing the blue solid line and the red dashed line. It is evident that the J·E within the ICS exhibits a much broader distribution than the ambient J·E, implying that the magnitude of J·E within the ICSs is generally higher than that in the ambient plasma.

Figure 10b compares the PDF of $J\cdot E'$ in the ICSs and the surrounding ambient plasma. We see that the intensity of energy dissipation in the ICSs is significantly greater than the background value (The average $J\cdot E'$ in the ICS is 0.14; The average $J\cdot E'$ in the ambient plasma is 0.002). In addition, the PDF is asymmetric with respect to $J\cdot E'=0$ with PDF($J\cdot E'>0$) is much larger than PDF($J\cdot E'<0$). This indicates that the average dissipation in the ICSs is positive, implying that the ICSs indeed contribute to the energy dissipation within the MBL.

6. Summary

The MBL is a complex region containing plasmas of the magnetosphere and magnetosheath. A large number of coherent structures, such as current sheets, current filaments, flux ropes, magnetic holes have frequently been observed in this region (Zhong et al., 2018; 2019). This paper focuses on the ICS, which includes both current sheet and filaments. We obtain the following main results based on a statistical investigation of more than 3,000 ICS, the threshold of which is 1.2 $\mu A/m^2$.

(1) The duration of the ICS is relatively short, mainly concentrated within 1 second. This corresponds to the thickness mostly below 1 d_i. The PDF of the temporal duration and thickness almost monotonically decreases with the increment of the duration and thickness.

(2) The ICS occurs predominantly within L = (8 -10) and in the dusk sector within MLT = (12 – 15). Most of the ICSs are located at the southern outflow region on the magnetosheath side in a boundary normal coordinate system.

(3) The current in the ICSs is mainly carried by electrons and mainly perpendicular to the magnetic field.

(4) The energy conversion is predominantly through the perpendicular current and electric field, while the energy dissipation (or non-ideal energy conversion) is mainly through the parallel current and electric field. This is due to that the perpendicular electric field is primarily the

electron convective electric field within the ICSs, i.e., the non-ideal electric field is mainly in the parallel direction.

(5) The energy conversion/dissipation in the ICSs is significantly greater than the ambient plasma. Besides, the plasma is accelerated and heated due to the overall positive value of $J \cdot E'$ in the ICSs.

MMS provides excellent opportunities to explore kinetic-scale structures and associated kinetics in our geospace. We demonstrate in this paper that the ICSs are essential for energy conversion in the MBL. It may be interesting to locate the ICSs in the reconnection geometry, for instance, how many of them are inside the diffusion region, magnetic flux rope, exhaust or separatrix region? Further efforts are also required to understand the exact physical mechanism responsible for the formation of these ICSs in the MBL.

Acknowledgement

We appreciate the MMS teams for the high-quality data and successful operation. This work is supported by the National Natural Science Foundation of China (NSFC) under grants 41774154 and 42074197. The data used in this study was obtained from the MMS Science Data Center (https://lasp.colorado.edu/mms/sdc/public/) and the OMNI website (https://spdf.gsfc.nasa.gov/pub/data/omni/omni.cdaweb/hro1min/)

Reference:

André, M., Vaivads, A., Buchert, S. C., Fazakerley, A. N., and Lahiff, A.

(2004). Thin electron-scale layers at the magnetopause. *Geophysical Research Letters*, 31(3). https://doi.org/10.1029/2003GL018137

Bale, S.D., Mozer, F.S., Phan, T. (2002) Observation of lower hybrid drift instability in the diffusion region at a reconnecting magnetopause. *Geophysical Research Letters.* 29, 33-1. https://doi.org/10.1029/2002GL016113

Berchem, J., Russell, C.T. (1982), The thickness of the magnetopause current layer – ISEE 1 and 2 observations. *Journal of Geophysical Research*, 87, 2108–2114. https://doi.org/10.1029/JA087iA04p02108

Borg, A. L., et al. (2005). Cluster encounter of a magnetic reconnection diffusion region in the near - Earth magnetotail on September 19, 2003. *Geophysical Research Letters*, 32(19). https://doi.org/10.1029/2005GL023794

Burch, J. L., Torbert, R. B., Phan, T. D., Chen, L. J., Moore, T. E., Ergun, R. E., et al. (2016). Electron-scale measurements of magnetic reconnection in space. *Science,* 352(6290), aaf2939. https://doi.org/10.1126/science.aaf2939

Burkholder, B. L., et al. (2020). Magnetospheric Multiscale Observation of an Electron Diffusion Region at High-Latitudes. *Geophysical Research Letters*, 47(15). https://doi.org/10.1029/2020GL087268

Chapman, S., and Ferraro, V. C. A. (1931). A new theory of magnetic storms. *Journal of Geophysical Research*, 36(2), 171–186. https://doi.org/10.1029/TE036i002p00077

Daughton, W. (1999). The unstable eigenmodes of a neutral sheet. *Physics of Plasmas*, 6(4), 1329–1343. https://doi.org/10.1063/1.873374

Daughton, W. (2003), Electromagnetic properties of the lower-hybrid drift instability in a thin current sheet, *Physics of Plasmas*, 10, 3103. https://doi.org/10.1063/1.1594724

Dunlop, M. W., Balogh, A., Glassmeier, K. -H., and Robert, P. (2002). Four-point Cluster application of magnetic field analysis tools: The Curlometer. *Journal of Geophysical Research*, 107, 1384. https://doi.org/10.1029/2001JA005088

Eastwood, J. P., et al. (2007). Multi-point observations of the Hall

electromagnetic field and secondary island formation during magnetic reconnection. *Journal of Geophysical Research*, 112. https://doi.org/10.1029/2006JA012158

Eastwood, J. P., Phan, T. D., Cassak, P. A., Gershman, D. J., Haggerty, C., Malakit, K., et al. (2016). Ion-scale secondary flux ropes generated by magnetopause reconnection as resolved by MMS. *Geophysical Research Letters*, 43, 4716–4724. https://doi.org/10.1002/2016GL068747

Elphic, R. C., and Russell, C. T. (1979). ISEE-1 and 2 magnetometer observations of the magnetopause. *ESASP*, 148, 43–50.

Ergun, R. E., Tucker, S., Westfall, J., Goodrich, K. A., Malaspina, D. M., Summers, D., et al. (2016). The axial double probe and fields signal processing for the MMS mission. *Space Science Reviews,* 199(1–4), 167–188. https://doi.org/10.1007/s11214-014-0115-x

Erickson, G. M., and R. A (1980). Wolf, Is steady convection possible in the Earth's magnetotail? *Geophysical Research Letters*., 7, 897. https://doi.org/10.1029/GL007i011p00897

Fu, H. S., Khotyaintsev, Y. V., Vaivads, A., André, M., and Huang, S. Y.

(2012). Electric structure of dipolarization front at sub-proton scale. *Geophysical Research Letters*, 39(6). https://doi.org/10.1029/2012GL051274

Fu, H. S., Vaivads, A., et al. (2017). Intermittent energy dissipation by turbulent reconnection. *Geophysical Research Letters*, 44(1), 37–43. https://doi.org/10.1002/2016GL071787

Hasegawa, H. (2012). Structure and Dynamics of the Magnetopause and Its Boundary Layers. *Monographs on Environment, Earth and Planets*, 1(2), 71–119. https://doi.org/10.5047/meep.2012.00102.0071

Huang, S. Y., Zhou, M., et al. (2012). Kinetic structure and wave properties associated with sharp dipolarization front observed by Cluster. *Annales Geophysicae*, 30(1), 97 – 107. https://doi.org/10.5194/angeo-30-97-2012

Huang, S. Y., Fu, H. S., Yuan, Z. G., Zhou, M., Fu, S., Deng, X. H., et al. (2015). Electromagnetic energy conversion at dipolarization fronts: Multispacecraft results. *Journal of Geophysical Research*, 120(6), 4496–4502. https://doi.org/10.1002/2015JA021083

552 Hwang, K. J., Sibeck, D. G., Giles, B. L., Pollock, C. J., Gershman, D.,
553 Avanov, L., et al. (2016). The substructure of a flux transfer event
554 observed by the MMS spacecraft. *Geophysical Research Letters*, 43,
555 9434–9443. https://doi.org/10.1002/2016GL070934
556
557 Hwang, K. J., et al. (2019). Electron Vorticity Indicative of the Electron
558 Diffusion Region of Magnetic Reconnection. *Geophysical Research*
559 *Letters*, 46(12), 6287–6296. https://doi.org/10.1029/2019GL082710
560
561 King, J. H., and Papitashvili, N. E. (2005). Solar wind spatial scales in
562 and comparisons of hourly Wind and ACE plasma and magnetic field
563 data. *Journal of Geophysical Research,* 110, A02104.
564 https://doi.org/10.1029/2004JA010649
565
566 Lapenta, G., Brackbill, J. U., and Daughton, W. S. (2003). The
567 unexpected role of the lower hybrid drift instability in magnetic
568 reconnection in three dimensions. *Physics of Plasmas*, 10(5), 1577–1587.
569 https://doi.org/10.1063/1.1560615
570
571 Le, G., and Russell, C.T. (1994), The thickness and structure of high beta
572 magnetopause current layer. *Geophysical Research Letters*. 21,
573 2451–2454. https://doi.org/10.1029/94GL02292

Lindqvist, P. A., Olsson, G., Torbert, R. B., King, B., Granoff, M., Rau, D., et al. (2016). The spin-plane double probe electric field instrument for MMS. *Space Science Reviews*, 199(1–4), 137–165. https://doi.org/10.1007/s11214-014-0116-9

Liu, C. M., Fu, H. S., et al. (2018). Electron-Scale Measurements of Dipolarization Front. *Geophysical Research Letters*, 45(10), 4628–4638. https://doi.org/10.1029/2018GL077928

Lu, S., Angelopoulos, V., Artemyev, A. V., Jia, Y., Chen, Q., Liu, J., and Runov, A. (2020). Magnetic reconnection in a charged, electron-dominant current sheet. *Physics of Plasmas*, 27(10), 102902. https://doi.org/10.1063/5.0020857

Man, H. Y., Zhou, M. et al, (2018). In Situ Observation of Magnetic Reconnection Between an Earthward Propagating Flux Rope and the Geomagnetic Field. *Geophysical Research Letters*, 45(17), 8729–8737. https://doi.org/10.1029/2018GL079778

Man, H. Y., Zhou, M., et al. (2020). Observations of Electron - Only Magnetic Reconnection Associated With Macroscopic Magnetic Flux

596 Ropes. *Geophysical Research Letters*, 47(19).
597 https://doi.org/10.1029/2020GL089659
598
599 Moser, A. L., and Bellan, P. M. (2012). Magnetic reconnection from a
600 multiscale instability cascade. *Nature*, 482, 379 – 381.
601 https://doi.org/10.1038/nature10827
602
603 Mozer, F. S., Bale, S. D., and Phan, T. D. (2002). Evidence of diffusion
604 regions at a subsolar magnetopause crossing. *Physical Review Letters*,
605 89(1), 15002. https://doi.org/10.1103/PhysRevLett.89.015002
606
607 Mozer, F. S., and Pritchett, P. L. (2009). Regions associated with electron
608 physics in asymmetric magnetic field reconnection. *Geophysical*
609 *Research Letters*, 36(7). https://doi.org/10.1029/2009GL037463
610
611 Nakamura, R., et al. (2002), Fast flow during current sheet thinning,
612 *Geophysical Research Letters,* 29(23), 2140,
613 https://doi.org/10.1029/2002GL016200
614
615 Nakamura, R., Varsani, A., et al. (2018). Multiscale Currents Observed by
616 MMS in the Flow Braking Region. *Journal of Geophysical Research*,
617 123(2), 1260–1278. https://doi.org/10.1002/2017JA024686
618

Nakamura, R., Genestreti, K. J., et al. (2019). Structure of the Current Sheet in the 11 July 2017 Electron Diffusion Region Event. *Journal of Geophysical Research : Space physics,* 124(2), 1173–1186. https://doi.org/10.1029/2018ja026028

Pan, D., Khotyaintsev, Y. V., et al, (2018). Rippled Electron-Scale Structure of a Dipolarization Front. *Geophysical Research Letters*, *45*(22), 12116–12124. https://doi.org/10.1029/2018GL080826

Phan, T. D., Eastwood, J. P., et al. (2016), MMS observations of electron-scale filamentary currents in the reconnection exhaust and near the X line. *Geophysical Research Letters*, 43(12), 6060–6069. https://doi.org/10.1002/2016GL069212

Phan, T. D., Eastwood, J. P., Shay, M. A., Drake, J. F., Sonnerup, B. Ö., Fujimoto, M., et al. (2018). Electron magnetic reconnection without ion coupling in Earth's turbulent magnetosheath. *Nature*, 557(7704), 202–206. https://doi.org/10.1038/s41586-018-0091-5

Pollock, C., Moore, T., Jacques, A., Burch, J., Gliese, U., Saito, Y., et al. (2016). Fast plasma investigation for magnetospheric multiscale. *Space Science Reviews,* 199(1–4), 331–406.

https://doi.org/10.1007/s11214-016-0245-4

Pu, Z. Y., J. Raeder, J. Zhong, Y. V. Bogdanova, M. Dunlop, C. J. Xiao, X. G. Wang, and A. Fazakerley (2013), Magnetic topologies of an in vivo FTE observed by Double Star/TC-1 at Earth's magnetopause, *Geophysical Research Letters,* 40, 3502–3506, https://doi.org/10.1002/grl.50714.

Pulkkinen, T. I. et al. (1999). Spatial extent and dynamics of a thin current sheet during the substorm growth phase on December 10, 1996. *Journal of Geophysical Research*, 104, 28475 – 28490. https://doi.org/10.1029/1999JA900240

Pulkkinen, T. I., and M. Wiltberger (2000), Thin current sheet evolution as seen in observations, empirical models, and MHD simulations, *Geophysical Research Letters,* 27, 1363. https://doi.org/10.1029/1999GL003726

Retinò, A., Sundkvist, D., Vaivads, A., Mozer, F., André, M., & Owen, C. J. (2007). In situ evidence of magnetic reconnection in turbulent plasma. *Nature Physics*, 3(4), 236–238. https://doi.org/10.1038/nphys574

663 Runov, A., Nakamura, R., Baumjohann, W., Zhang, T. L., Volwerk, M.,
664 Eichelberger, H.-U., and Balogh, A. (2003). Cluster observation of a
665 bifurcated current sheet. *Geophysical Research Letters*, 30(2), 1036.
666 https://doi.org/10.1029/2002GL016136
667
668 Runov, A., et al. (2009). THEMIS observations of an
669 earthward-propagating dipolarization front. *Geophysical Research*
670 *Letters*, 36(14). https://doi.org/10.1029/2009GL038980
671
672 Russell, C. T., Mellott, M. M., Smith, E. J., & King, J. H. (1983).
673 Multiple spacecraft observations of interplanetary shocks: Four spacecraft
674 determination of shock normals. *Journal of Geophysical Research,*
675 88(A6), 4739–4748. https://doi.org/10.1029/JA088iA06p04739
676
677 Russell, C. T., Anderson, B. J., Baumjohann, W., Bromund, K. R.,
678 Dearborn, D., Fischer, D., et al. (2016). The Magnetospheric Multiscale
679 magnetometers. *Space Science Reviews,* 199(1–4), 189–256.
680 https://doi.org/10.1007/s11214-014-0057-3
681
682 Sergeev, V., Runov, A., et al. (2003). Current sheet flapping motion and
683 structure observed by Cluster. *Geophysical Research Letters*, 30(6),
684 1327. https://doi.org/10.1029/2002GL016500

685

686 Sergeev, V., Angelopoulos, V., Apatenkov, S., Bonnell, J., Ergun, R.,
687 Nakamura, R., McFadden, J., Larson, D., and Runov, A (2009), Kinetic
688 structure of the sharp injection/dipolarization front in the flow-braking
689 region, *Geophysical Research Letters*, 36, L21105,
690 doi:10.1029/2009GL040658.

691

692 Schindler, K., and Birn, J. (1982). Self - consistent theory of time -
693 dependent convection in the Earth's magnetotail. *Journal of Geophysical*
694 *Research*, 87, 2263–2275. https://doi.org/10.1029/JA087iA04p02263

695

696 Shue, J.-H., Chao, J. K., Fu, H. C., Russell, C. T., Song, P., Khurana, K.
697 K., and Singer, H. J. (1997). A new functional form to study the solar
698 wind control of the magnetopause size and shape. *Journal of*
699 *Geophysical Research*, 102, 9497–9511.
700 https://doi.org/10.1029/97JA00196

701

702 Torbert, R. B., Russell, C. T., Magnes, W., Ergun, R. E., Lindqvist, P. A.,
703 LeContel, O., et al. (2016). The FIELDS instrument suite on MMS:
704 Scientific objectives, measurements, and data products. *Space Science*
705 *Reviews,* 199(1–4), 105–135. https://doi.org/10.1007/s11214-014-0109-8

706

Torbert, R. B., Burch, J. L., Phan, T. D., et al. (2018). Electron-scale dynamics of the diffusion region during symmetric magnetic reconnection in space. *Science*, 362(6421), 1391–1395. https://doi.org/10.1126/science.aat2998

Tsyganenko, N. A. (1995). Modeling the Earth's magnetospheric magnetic field confined within a realistic magnetopause. *Journal of Geophysical Research,* 100(A4), 5599–5612. https://doi.org/10.1029/94JA03193

Vaivads, A., André, M., Buchert, S. C., Wahlund, J. - E., Fazakerley, A. N., and Cornilleau - Wehrlin, N. (2004). Cluster observations of lower hybrid turbulence within thin layers at the magnetopause. *Geophysical Research Letters*, 31(3). https://doi.org/10.1029/2003GL018142

Vogiatzis, I. I.; Isavnin, A.; Zong, Q.-G.; Sarris, E. T.; Lu, S. W.; Tian, A. M. (2015). Dipolarization fronts in the near-Earth space and substorm dynamics. *Annales Geophysicae*, 33(1), 63–74. https://doi.org/10.5194/angeo-33-63-2015

Wang, S., Chen, L., et al. (2019). Observational Evidence of Magnetic Reconnection in the Terrestrial Bow Shock Transition

729 Region. *Geophysical Research Letters*, 46(2), 562–570.
730 https://doi.org/10.1029/2018GL080944.
731
732 Wang, S., Wang, R., Lu, Q., Fu, H., and Wang, S. (2020). Direct evidence
733 of secondary reconnection inside filamentary currents of magnetic flux
734 ropes during magnetic reconnection. *Nature Communications*, 11(1), 1–8.
735 https://doi.org/10.1038/s41467-020-17803-3
736
737 Webster, J. M., Burch, J. L., et al. (2018), Magnetospheric Multiscale
738 Dayside reconnection electron diffusion region events. *Journal of*
739 *Geophysical Research: Space Physics,* 123, 4858–4878.
740 https://doi.org/10.1029/2018JA025245
741
742 Yi, Y., Zhou, M., Song, L., & Deng, X. (2019). On the Energy
743 Conversion Rate during Collisionless Magnetic Reconnection. *The*
744 *Astrophysical Journal*, 883(1).https://doi.org/10.3847/2041-8213/ab40c1
745
746 Zenitani, S., Hesse, M., Klimas, A., Black, C., and Kuznetsova, M. (2011).
747 The inner structure of collisionless magnetic reconnection: The
748 electron-frame dissipation measure and Hall fields. *Physics of Plasmas*,
749 18(12), 122108–122108. https://doi.org/10.1063/1.3662430
750

751 Zhao, C., Russell, C. T., Strangeway, R. J., Petrinec, S. M., Paterson, W.
752 R., Zhou, M., et al. (2016). Force balance at the magnetopause
753 determined with MMS: Application to flux transfer events. *Geophysical*
754 *Research Letters*, 43, 11, 941–11, 947.
755 https://doi.org/10.1002/2016GL071568
756
757 Zhong, Z. H., Tang, R. X., Zhou, M., Deng, X. H., et al. (2018). Evidence
758 for Secondary Flux Rope Generated by the Electron Kelvin-Helmholtz
759 Instability in a Magnetic Reconnection Diffusion Region. *Physical*
760 *Review Letters*, 120(7), 75101.
761
762 Zhong, Z. H., Zhou, M., Huang, S. Y., Tang, R. X., Deng, X. H., Pang, Y.,
763 and Chen, H. T. (2019). Observations of a kinetic-scale magnetic hole in
764 a reconnection diffusion region. Geophysical Research Letters,
765 46.https://doi.org/10.1029/2019GL082637
766
767 Zhou, M., Ashour-Abdalla, M., Deng, X., Schriver, D., El-Alaoui, M.,
768 and Pang, Y. (2009). THEMIS observation of multiple dipolarization
769 fronts and associated wave characteristics in the near-Earth
770 magnetotail. *Geophysical Research Letters*, 36(20).
771 https://doi.org/10.1029/2009GL040663
772

773 Zhou, M., Li, H., Deng, X., et al. (2014). Characteristic distribution and
774 possible roles of waves around the lower hybrid frequency in the
775 magnetotail reconnection region. *Journal of Geophysical Research*,
776 119(10), 8228–8242. https://doi.org/10.1002/2014JA019978
777
778 Zhou, M., Ashour-Abdalla, M. et al. (2016), Observation of
779 high-frequency electrostatic waves in the vicinity of the reconnection ion
780 diffusion region by the spacecraft of the Magnetospheric Multiscale
781 (MMS) mission. *Geophysical Research Letters,* 43(10), 4808–4815.
782 https://doi.org/10.1002/2016GL069010
783
784 Zhou, M., Berchem, J., Walker, R. J., el Alaoui, M., Deng, X., Cazzola, E.,
785 et al. (2017). Coalescence of macroscopic flux ropes at the subsolar
786 magnetopause: Magnetospheric Multiscale observations. *Physical Review*
787 *Letters*, 119(5), 055101. https://doi.org/10.1103/PhysRevLett.119.055101
788
789 Zhou, M., Huang, J., et al. (2019a), Electron-scale Vertical Current Sheets
790 in a Bursty Bulk Flow in the Terrestrial Magnetotail. *The Astrophysical*
791 *Journal*, 872(2).
792
793 Zhou, M., Deng, X. H., et al. (2019b). Observations of an Electron
794 Diffusion Region in Symmetric Reconnection with Weak Guide

Field. *The Astrophysical Journal*, 870(1), 34.

Zhou, M., Man, H. Y., Deng, X. H., Pang, Y., Khotyaintsev, Y., Lapenta, G., et al. (2021). Observations of secondary magnetic reconnection in the turbulent reconnection outflow. *Geophysical Research Letters*, 48, e2020GL091215. https://doi.org/10.1029/2020GL091215

Figure 1:

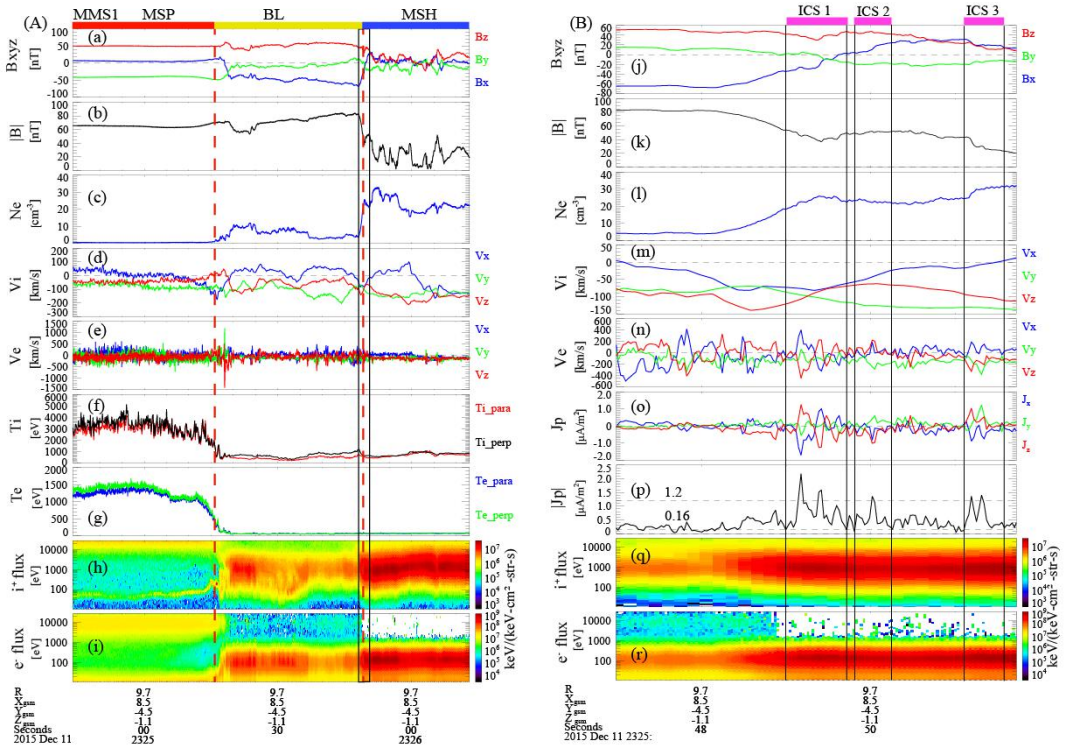

Figure 1. An example of a burst mode interval containing the MBL observed by MMS1 between 23:24:24 UT and 23:26:23 UT. (a) Three components of the magnetic fields; (b) magnetic field strength; (c) electron number density; (d) three components of the ion bulk velocity; (e) three components of the electron bulk velocity; (f) ion and (g) electron temperature; (h) ion and (i) electron omnidirectional differential energy flux. Panels (j) to (r) display the expanded view of MMS1 observations around the

ICSs. (j) Three components of the magnetic fields; (k) magnetic field strength; (l) electron number density; (m) ion bulk velocity; (n) electron bulk velocity; (o) three components of the current density calculated from the plasma moments, i.e., $J_p = n_e q(V_i - V_e)$, where n_e is the electron number density, q is the unit charge, V_i and V_e are the ion and electron bulk velocity, respectively; (p) magnitude of the current density, namely $|Jp| = \sqrt{Jp_x^2 + Jp_y^2 + Jp_z^2}$, where Jp_x, Jp_y and Jp_z are the three components of the current density; (q) ion and (r) electron omnidirectional differential energy flux. Vectors are displayed in the GSM coordinate system. The magenta bars at the top of Figure 1B highlight the three ICSs.

Figure 2:

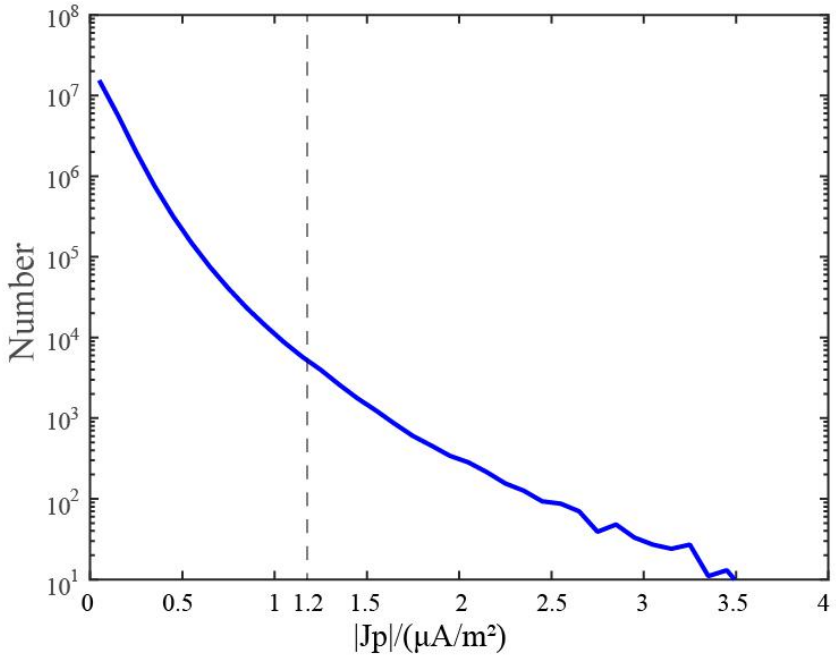

Figure 2. The number of data points as a function of |Jp| from all the burst mode intervals containing the MBL, here $|Jp| = \sqrt{Jp_x^2 + Jp_y^2 + Jp_z^2}$ is the total current density. Each data point has a temporal resolution of 0.03 s. We choose 1.2 μA/m^2 as the threshold for the ICS since 1.2 μA/m^2 is about 10 times the standard deviation of the Jp distribution shown in this plot.

Figure 3:

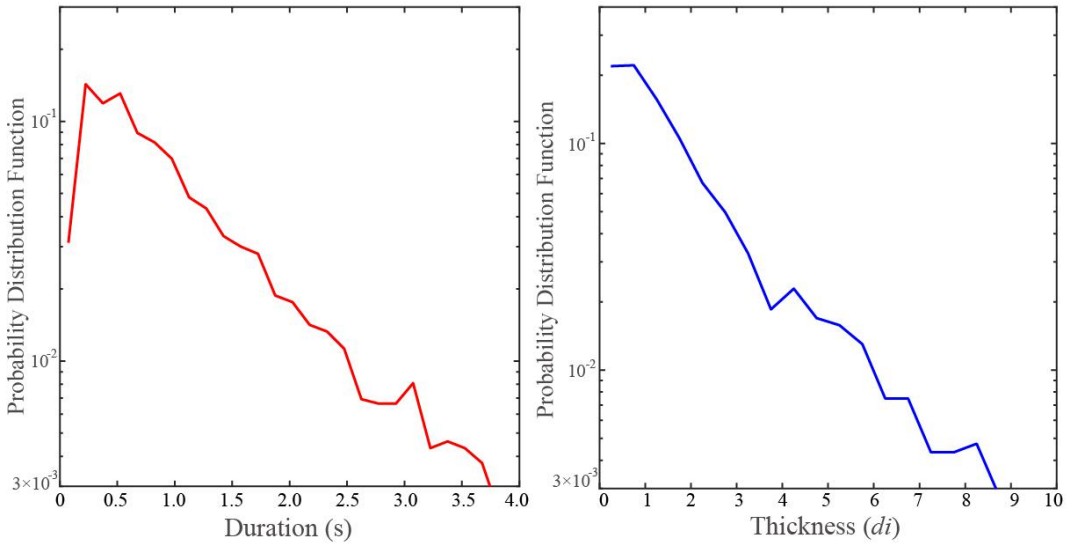

Figure 3. (a) PDF of the temporal duration for all the ICSs in the dayside MBL. (b) PDF of the normalized thickness of the ICSs, which was observed by all the four MMS spacecraft, and the cross-correlation coefficient among the four spacecraft is higher than 0.9.

Figure 4:

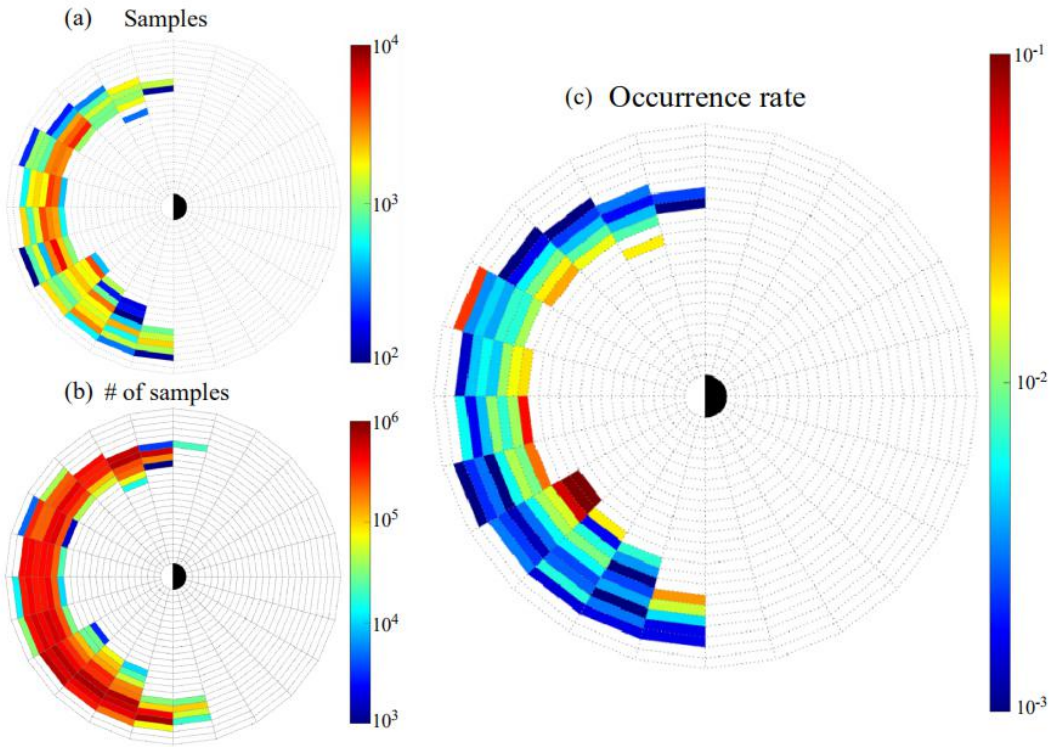

Figure 4. Global distribution of (a) all valid ICSs samples; (b) total number of samples of MMS1 during the burst mode intervals containing the dayside MBL; (c) occurrence rate of the ICSs. All the results are shown in the L-MLT (0.5 L × 1 MLT) coordinate for L = 0 -13. From left to right, each cell represents 0.5 L viewing from

the North Pole.

Figure 5:

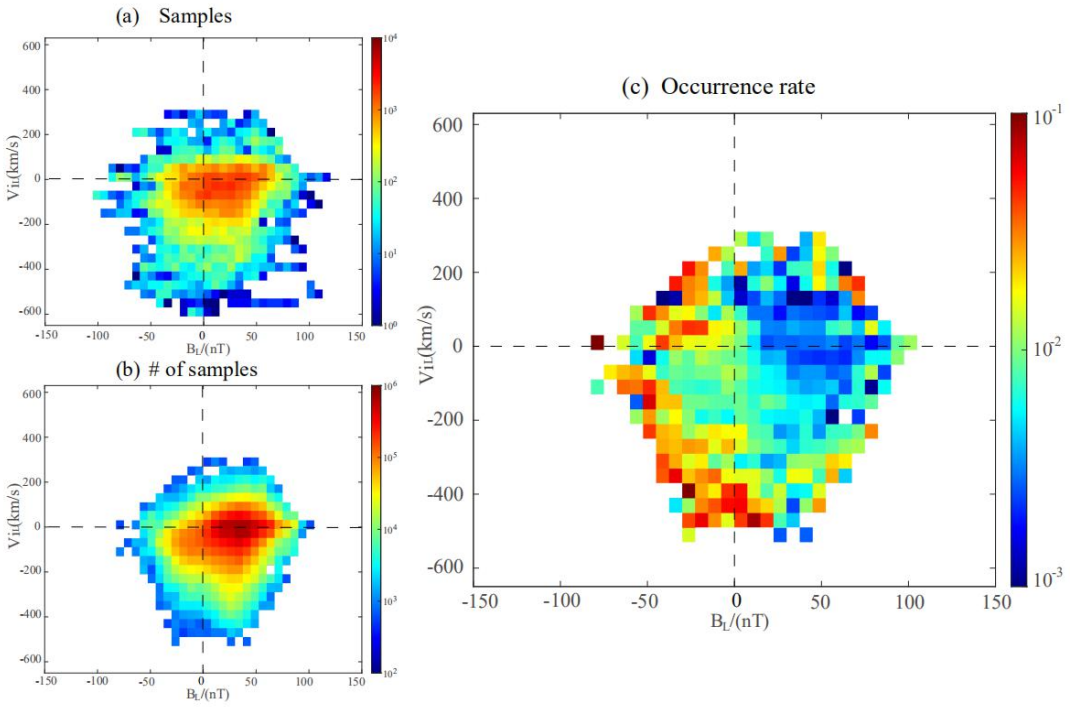

Figure 5. Local distribution of (a) all valid ICSs samples; (b) total number of samples of MMS1 during the burst mode intervals containing the dayside MBL; (c) occurrence rate of the ICSs. All of the results are shown in the B_L-V_{iL} plane in the local boundary normal coordinate.

Figure 6:

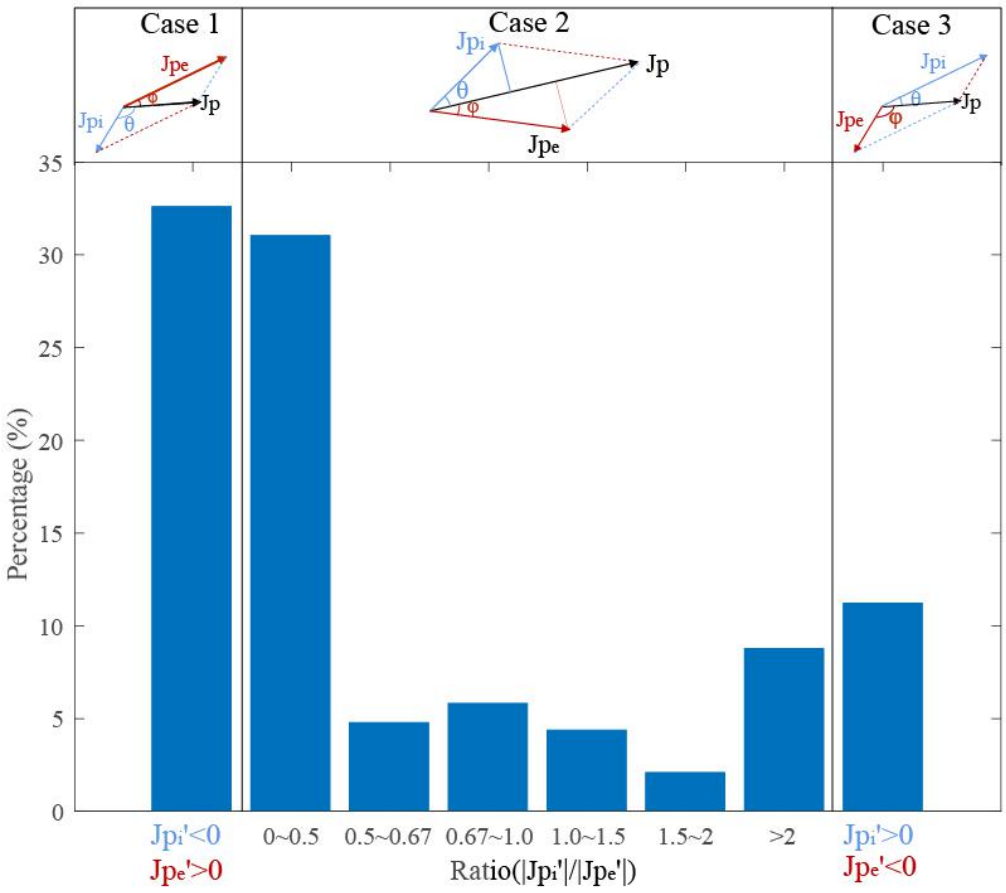

Figure 6. Histogram of the proportion of electron current and ion current in the total

current. The schematic at the top is a visual representation of the current composition in three different situations.

Figure 7:

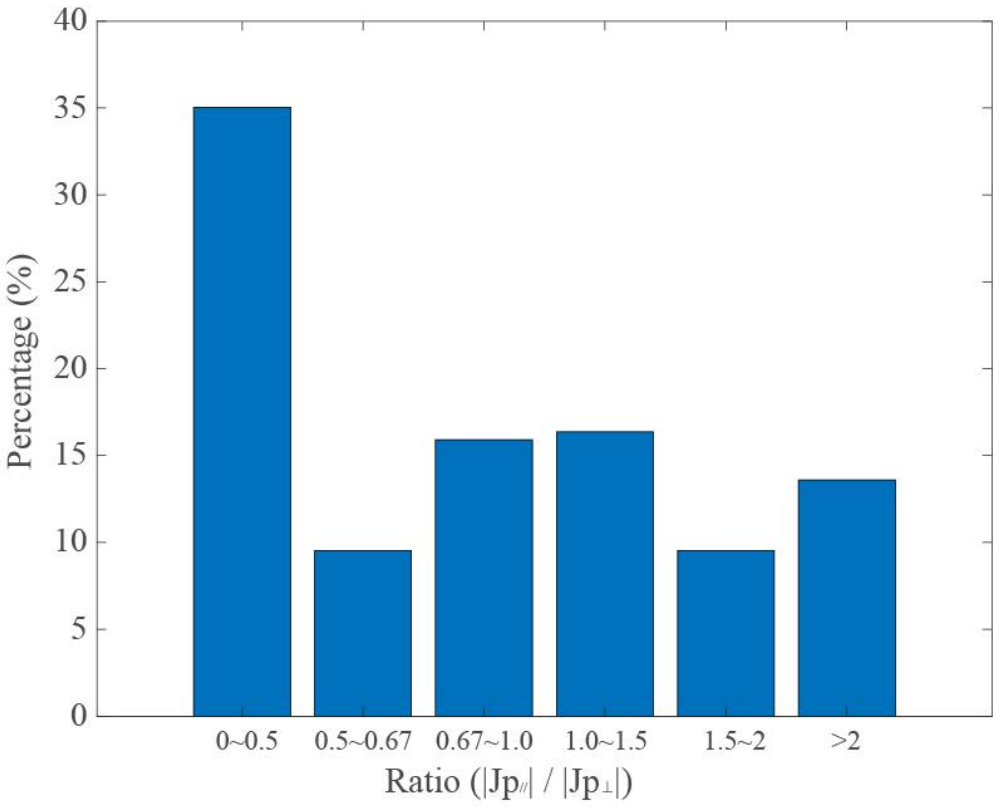

Figure 7. Histogram of the proportion of the ratio of the parallel current ($Jp_{//}$) to the perpendicular current ($Jp_{\perp}$).

Figure 8:

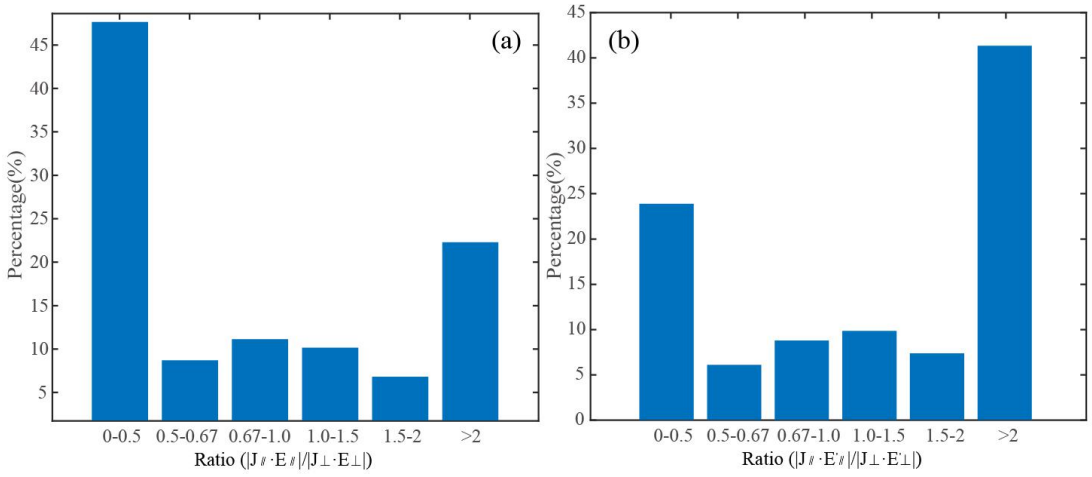

Figure 8. Histogram of the proportion of (a) $|J_{//}\cdot E_{//}|/|J_{\perp}\cdot E_{\perp}|$ and (b) $|J_{//}\cdot E'_{//}|/|J_{\perp}\cdot E'_{\perp}|$.

Figure 9:

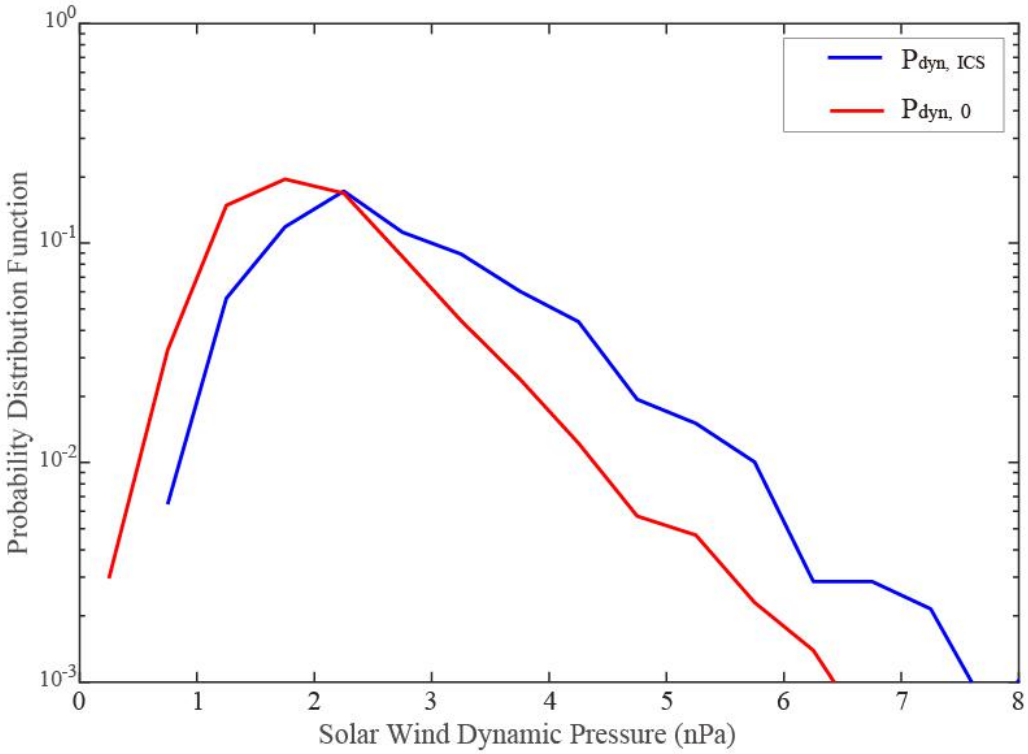

Figure 9. PDF of the $P_{dyn,ICS}$ (blue curve) and $P_{dyn,0}$ (red curve).

974

975

976

977

978

979

980

981

982

983 **Figure 10:**

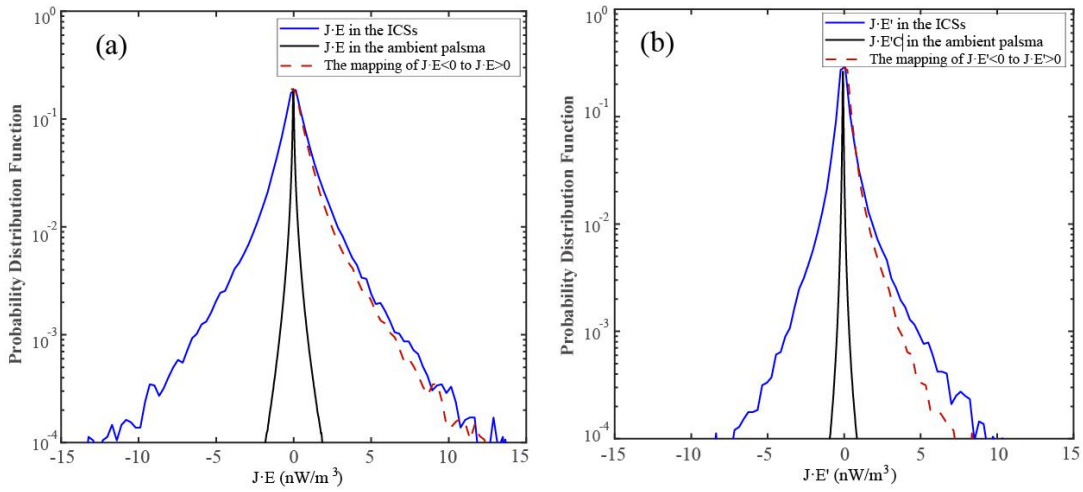

984

985 **Figure 10.** PDF of $J \cdot E$ (a) and $J \cdot E'$ (b) within the ICSs (blue curve) and ambient
986 plasma in the MBL excluding the ICSs (black curve). The red dotted line is the
987 mirrored part of the distribution with $J \cdot E<0$. Each sample in this plot has a cadence of
988 0.03 s.

989